

ADJOINT-BASED OPTIMIZATION AND INVERSE DESIGN OF PHOTONIC
DEVICES

A DISSERTATION
SUBMITTED TO THE DEPARTMENT OF APPLIED PHYSICS
AND THE COMMITTEE ON GRADUATE STUDIES
OF STANFORD UNIVERSITY
IN PARTIAL FULFILLMENT OF THE REQUIREMENTS
FOR THE DEGREE OF
DOCTOR OF PHILOSOPHY

Tyler William Hughes
June 2019

© Copyright by Tyler William Hughes 2019
All Rights Reserved

I certify that I have read this dissertation and that, in my opinion, it is fully adequate in scope and quality as a dissertation for the degree of Doctor of Philosophy.

(Shanhui Fan) Principal Adviser

I certify that I have read this dissertation and that, in my opinion, it is fully adequate in scope and quality as a dissertation for the degree of Doctor of Philosophy.

(Robert L. Byer)

I certify that I have read this dissertation and that, in my opinion, it is fully adequate in scope and quality as a dissertation for the degree of Doctor of Philosophy.

(Olav Solgaard)

I certify that I have read this dissertation and that, in my opinion, it is fully adequate in scope and quality as a dissertation for the degree of Doctor of Philosophy.

(Mark Brongersma)

I certify that I have read this dissertation and that, in my opinion, it is fully adequate in scope and quality as a dissertation for the degree of Doctor of Philosophy.

(Amir Safavi-Naeini)

Approved for the Stanford University Committee on Graduate Studies

Preface

This thesis tells you everything you need to know about...

Acknowledgments

I would like to thank ...

Contents

Preface	iv
Acknowledgments	v
1 Introduction	1
1.1 Photonics	1
1.2 Designing of Photonic Devices	2
1.2.1 Traditional Design Approach	2
1.2.2 Inverse Design Approach	2
1.3 Introduction to Adjoint Method	3
1.4 Thesis Overview	4
2 Adjoint-Based Optimization of Accelerator on a Chip	5
2.1 Dielectric Laser Acceleration	5
2.2 Adjoint Method for Particle Accelerators	7
2.3 Inverse design of Dielectric Laser Accelerator	13
2.4 Optimization of acceleration factor	18
2.5 Conclusions	20
3 Integrated Photonic Circuit for Accelerators on a Chip	22
3.1 Motivation	22
3.2 On-Chip Laser Coupling Device	22
3.3 Parameter Study	22
3.4 Automatic Controlled Power Delivery Systems	22
3.4.1 Phase Control Mechanism	22
3.4.2 Power Control Mechanism using Reconfigurable Circuit	22
3.5 Experimental Efforts	22
3.5.1 Waveguide Damage and Nonlinearity Measurements	22
3.5.2 Demonstration of Waveguide-Coupled Acceleration	22

4	Training of Optical Neural Networks	23
4.1	Introduction to Machine Learning	24
4.1.1	Applications	24
4.1.2	Hardware Demands	24
4.2	Linear Nanophotonic Processors	24
4.3	Optical Neural Networks	24
4.3.1	Conventional Neural Network	24
4.3.2	Optical Integration	24
4.3.3	Training Protocols	24
4.4	In Situ Backpropagation Training	24
4.4.1	Derivation Using Adjoint Method	24
4.4.2	Method for Measurement of Adjoint Gradient	24
4.4.3	Numerical Demonstrations	24
4.5	Electro-Optic Activation Functions	24
4.5.1	Motivation	24
4.5.2	Proposed Activation Function	24
4.5.3	Scaling Laws	24
4.5.4	Demonstration	24
4.6	Wave-Based Analog Recurrent Neural Networks	24
4.6.1	Wave Equation vs. Recurrent Neural Network	24
4.6.2	Vowel Classification through Wave Propagation	24
5	Extension of Adjoint Method beyond Linear Time-Invariant Systems.	25
5.1	Nonlinear Devices	25
5.1.1	Generalization of Adjoint Method to Nonlinear Problems	25
5.1.2	Inverse Design of Nonlinear Photonic Switches	25
5.2	Active Devices	25
5.2.1	Adjoint Sensitivity for Multi-Frequency FDFD Problems	25
5.2.2	Inverse Design of Optical Isolators through Dynamic Modulation	25
5.3	Adjoint for Time Domain	25
5.3.1	Derivation	25
5.3.2	Challenges	25
5.4	Forward-mode Differentiation	25
6	Conclusion and Final Remarks	26
A	Something	27

List of Tables

2.1	Acceleration factor (f_A) before and after maximization.	20
-----	--	----

List of Figures

2.1	Diagram outlining the system setup for side-coupled DLA with an arbitrary dielectric structure $\epsilon(x, y)$ (green). A charged particle moves through the vacuum gap with speed βc_0 . The periodicity is set at $\beta\lambda$ where λ is the central wavelength of the laser pulse.	6
2.2	Definition of the vector field, $\vec{\eta}$, which defines the position of the electron in the frequency domain. The green regions represent domains where we will optimize the material properties using the adjoint method. The central gap is constrained to vacuum to allow passage of the electron beam. The red arrow signifies the driving laser.	9
2.3	Demonstration of adjoint method in calculating accelerator sensitivities. (a) The acceleration gradient (G) of a square accelerator structure (inset) as a function of the square's relative permittivity. We express the acceleration gradient in its dimensionless form, normalized by the electric field amplitude of the incident plane wave (E_0). The particle traverses along the dotted line with a velocity of c_0 ($\beta = 1$) and a plane wave is incident from the bottom of the structure. (b) The sensitivity $\frac{dG}{d\epsilon}$ of the gradient with respect to changing the square relative permittivity for direct central difference (solid line) $\frac{dG}{d\epsilon} = \frac{G(\epsilon+\Delta\epsilon)-G(\epsilon-\Delta\epsilon)}{2\Delta\epsilon}$ and using the adjoint method (circles). The two calculations agree with excellent precision. The dotted line at $\frac{dG}{d\epsilon} = 0$, corresponds to local minima and maxima of $G(\epsilon)$ above.	14
2.4	Optimization routine for DLA.	15

2.5	Demonstration of the structure optimization for $\beta = 0.5$, laser wavelength $\lambda = 2\mu\text{m}$, and a gap size of 400 nm. A plane wave is incident from the bottom in all cases. (a) Acceleration gradient as a function of iteration number for different maximum relative permittivity values, corresponding to those of Si, Si_3N_4 , and SiO_2 at the laser wavelength. The acceleration gradient is normalized by the electric field amplitude of the incident plane wave (E_0). The optimizations converge after about five-hundred iterations. (b-d) Final structure permittivity distributions (white = vacuum, black = ϵ_m) corresponding to the three curves in (a). Eight periods are shown, corresponding to four laser wavelengths. For each (b-d), design region widths on each side of the particle gap were given by 1, 2, and $4\mu\text{m}$ for Si, Si_3N_4 , and SiO_2 , respectively. . . .	16
2.6	Similarity between DLA structures designed using adjoint method (left) and those independently proposed using human intuition.	17
2.7	Demonstration of the final structures after optimization for (a) maximizing gradient only, (b) maximizing the acceleration factor. $\beta = 0.5$, laser wavelength $\lambda = 2\mu\text{m}$, gap size of 400 nm. $\epsilon_m = 2.1$, corresponding to SiO_2 . In (a), the high gradients are achieved using reflective dielectric mirrors to confine and enhance the fields in the center region. In (b), these dielectric mirrors are removed and the pillar structures are augmented. The structure in (b) shows a 23% increase in the acceleration factor in the material region when compared to (a).	19

Chapter 1

Introduction

1.1 Photonics

The field of photonics is concerned with the study and manipulation of light. This endeavor has given rise to countless technologies of great practical and scientific interest. Most prominently, the use of light as an information carrier has enabled high speed and low loss communications through the use of optical fiber technologies [2]. Light is also used extensively for precise detection and measurement in scientific studies. For example, X-ray radiation is now used to observe femtosecond dynamics in chemical reactions [21], and laser interferometry was recently used to measure gravitational waves emitted from black hole mergers [27]. Apart from these, there are many applications of photonics with significant practical importance ranging from renewable energy [9, 48] to passive refrigeration [40, 17].

One of the most important achievements of photonics in the past few decades has been the development of *integrated* photonic devices [39]. In this paradigm, rather than constructing devices using macroscopic components, such as lenses and mirrors, they are created on the surface of a chip using techniques common to the semiconductor industry. Such an approach is appealing as it allows for compact, low cost, and highly functional devices that are also easier to integrate with existing electronic platforms based on composite metal on semiconductor (CMOS) technology [46]. The field of ‘Silicon photonics’ has especially generated much interest in recent years, in which photonic devices integrated on Silicon are employed in applications ranging from optical interconnects for fast data transfer between microchips to large scale integrated photonic circuits [18].

Here, we will primarily explore two emerging technologies based on integrated photonics, (1) Laser-driven particle accelerators on a chip, and (2) optical hardware for machine learning applications. The approach to laser-driven particle acceleration examined here is referred to as ‘dielectric laser acceleration’, in which charged particles are accelerated by the near field of a patterned dielectric structure driven by an external laser. As we will show, this technology may benefit greatly from

the use of integrated photonic platforms for its eventual practical applications. Integrated photonics is also a promising candidate for building hardware platforms specialized on machine learning tasks. As the transmission of an image through an optical lens passively performs a Fourier transform, reconfigurable integrated photonic devices are capable of performing arbitrary linear operations through pure transmission of optical signals through their domain. As machine learning models are often dominated by linear operations, this technology may provide a platform with higher processing speed, lower energy usage when compared to conventional digital electronics.

1.2 Designing of Photonic Devices

1.2.1 Traditional Design Approach

In any of these applications, the design of the photonic device is of critical importance. The typical approach to such a process is to use physical intuition to propose an initial structure. This structure may be parameterized by several *design variables*, such as geometric or material parameters. These parameters may then be optimized, using numerical simulation or experiment, until convergence on a functioning device that further satisfies fabrication constraints, such as minimum feature size, for example. As an example, if one is interested in designing a device that routes input light to different ports for different input wavelengths, one such approach would be to combine several wavelength filters into one device and tune their parameters until the functionality is achieved. Such an approach, while intuitive, has a number of potential drawbacks. First, it is dependent on the designer having significant physical intuition about the problem, which is not always available especially in novel applications. Second, the method of tuning parameters by hand is tedious and the time needed to complete such a task generally scales exponentially with the number of design variables. This fact means that the designer is practically limited to examining a small number of design variables or only a few select combinations. The use of few design variables further limits the designer to consider devices within a fixed parameterization. For example, if one were to design a device for tailored diffraction or transmission characteristics, he or she may decide to explore grating structures parameterized by tooth height, width, and duty cycle, while ignoring other possible designs.

1.2.2 Inverse Design Approach

Inverse design is a radically different approach that has become popularized in photonics within the past decade [31]. In this scheme, the overall performance of the device is defined mathematically through an *objective function*, which is then either maximized or minimized using computational and mathematical optimization techniques. This approach allows for automated design of photonic devices that are often more compact and higher performance than their traditionally designed alternatives. Furthermore, this approach allows one to search through a much larger parameter space,

typically on the order of thousands to millions of design variables, which allows the design algorithms to often find structures with complexities often extending beyond the intuition of the designer.

The use of inverse design has a long history in other fields, such as mechanics [45], aerodynamics [19], and heat transfer [34]. However, in the past decade, it has been applied successfully to many photonics problems. A few early examples include the use of inverse design to engineer wavelength splitters [36, 23], perfect 90 degree bends in dielectric waveguides [20], or the design of photonic crystals [6]. More recently, it was applied to engineer more exotic phenomena, such as the photonic crystal band structure [PhC band], nonlinear optical responses [28], and metamaterials [42]. For a thorough overview of the progress of inverse design in photonics at the time of publishing, we refer the reader to Ref. 31.

1.3 Introduction to Adjoint Method

As we will explore in detail, the ability to perform inverse design is largely enabled by the ability to efficiently search such a large parameter space. Typically, this is performed using *gradient-based optimization* techniques, which use local gradient information to iteratively progress through the design space. In design problems with several degrees of freedom, gradient-based methods typically converge on local minima much faster than more general optimization techniques such as particle swarm optimization [1] or genetic algorithms [47], which don't typically use local gradient information.

In problems constrained by physics described by linear systems or differential equations, the *adjoint method* is used to compute these gradients. The adjoint method allows one to compute gradients of the objective function with respect to each of the design parameters in a complexity that is (in practice) independent on the size of the design space. As such, it is the cornerstone of the inverse design works in photonics and other fields.

Here we give a brief introduction to the mathematics behind the adjoint method. Many engineering systems can be described by a linear system of equations $A(\phi)\mathbf{x} = \mathbf{b}$, where A is a sparse matrix that depends on a set of parameters describing the system, ϕ . Solving this equation with source \mathbf{b} results in the solution \mathbf{x} , from which an objective function $J = J(\mathbf{x})$ can be computed.

The optimization of this system corresponds to maximizing or minimizing J with respect to the set of parameters ϕ . For this purpose, the adjoint method allows one to calculate the gradient of the objective function $\nabla_{\phi} J$ for an arbitrary number of parameters. Crucially, this gradient may be obtained with the computational cost of solving only one additional linear system $\hat{A}^T \bar{\mathbf{x}} = -\frac{\partial J}{\partial \mathbf{x}}^T$, which is often called the 'adjoint' problem.

As we will show, this method may be readily applied to the inverse design of electromagnetic devices. In this case, A represents Maxwell's equations describing the device, \mathbf{x} are the electromagnetic fields, and \mathbf{b} is the electric current source driving the system.

1.4 Thesis Overview

Like inverse design, the adjoint method has been known in the applied math community for quite some time, and has been applied to numerous other fields. Its application to photonics is quite recent, but has had a significant impact. In this thesis, we will discuss the application of the adjoint method to new applications in photonics. We will also introduce extensions to the adjoint method, which allow it to be applied to new systems and implemented experimentally. The thesis is organized as follows. In Chapter 2, we will introduce the mathematical details behind adjoint-based optimization. To give a concrete example, we will focus on its application to laser-driven particle accelerators on a chip. To continue this discussion, in Chapter 3, we will discuss the scaling of laser-driven particle accelerators to longer length scales using photonic integrated circuits. This discussion will motivate the need to use inverse design for new components, and we will discuss efforts to use such techniques to build these systems experimentally. In Chapter 4, we will discuss optical hardware platforms for machine learning applications. The adjoint method will be explored in the context of training an optical neural network, and we will show that its implementation corresponds to the backpropagation algorithm of conventional neural networks. A novel method for experimentally measuring the gradients obtained through the adjoint method will be introduced in the context of machine learning hardware and we will also discuss our exploration of nonlinear optical activation functions and time-domain machine learning processing using wave physics. In Chapter 5, we will explore the extension of the adjoint method to new scenarios in photonics, namely nonlinear and periodically modulated systems. We will conclude in Chapter 6.

Chapter 2

Adjoint-Based Optimization of Accelerator on a Chip

2.1 Dielectric Laser Acceleration

In the public sphere, particle accelerators most commonly conjure images of giant particle colliders, such as the Large Hadron Collider. However, most particle accelerators are used in other applications, such as radiotherapy, X-ray generation, and ion implantation for semiconductor device fabrication [14]. Conventional radio-frequency (RF) accelerators use a metal or superconducting cavity, driven with microwave radiation, to provide sustained acceleration to charged particles traversing the structure. However, the available acceleration per length is fundamentally limited by the material breakdown and damage of the cavity. Therefore, for an accelerator driven at its damage threshold, the only option to achieve high total energy gains is to make the device longer. The largest current particle accelerators reach several of kilometers in length, requiring substantial resources to operate and maintain.

Dielectric laser acceleration (DLA) is an emerging method that seeks to revolutionize particle accelerator technology by exploiting decades of progress in nanofabrication, materials science, and laser technology. In DLA, periodic dielectric structures are illuminated with infrared laser light, which creates an electromagnetic field pattern in their vicinity that can accelerate electrically charged particles, such as electrons. When compared to metal surfaces at microwave frequencies, dielectric materials have very high damage thresholds at short pulse durations and infrared wavelengths [29, 43]. This allows DLAs to achieve energy gains per length that are 1 to 2 orders of magnitude higher than those found in conventional radio frequency (RF) accelerators. Experimental demonstrations of these acceleration gradients have been made practical in recent years by the availability of robust nanofabrication techniques combined with modern solid state laser systems [13].

As a result, the development of DLA can lead to compact particle accelerators that enable new applications. By providing the potential for generating relativistic electron beams in relatively short length scales, DLA technology is projected to have numerous applications where tabletop accelerators may be useful, including medical imaging, radiation therapy, and X-ray generation [37, 14]. To achieve high energy gain in a compact size, it is of principle interest to design structures that may produce the largest acceleration gradients possible without exceeding their respective damage thresholds.

Several recently demonstrated candidate DLA structures consist of a planar dielectric structure that is periodic along the particle axis with either an semi-open geometry or a narrow (micron to sub-micron) vacuum gap in which the particles travel [38, 35, 29, 26, 10, 7, 8, 24]. These structures are then side-illuminated by laser pulses. Fig. ?? shows a schematic of the setup, with a laser pulse incident from the bottom.

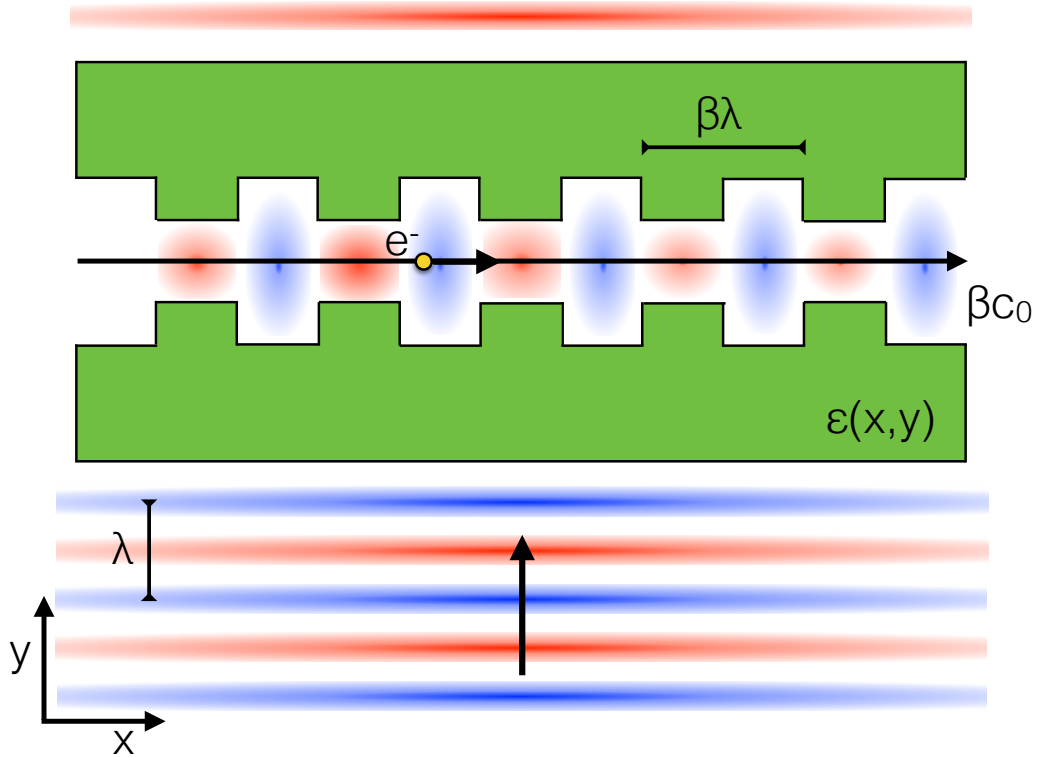


Figure 2.1: Diagram outlining the system setup for side-coupled DLA with an arbitrary dielectric structure $\epsilon(x, y)$ (green). A charged particle moves through the vacuum gap with speed βc_0 . The periodicity is set at $\beta\lambda$ where λ is the central wavelength of the laser pulse.

The laser field may also be treated with a pulse front tilt [16, 3] to enable group velocity matching over a distance greater than the laser's pulse length. For acceleration to occur, the dielectric structure must be designed such that the particle feels an electric field that is largely parallel to its trajectory over many optical periods. In the following calculations, the geometry of the dielectric structure is represented by a spatially varying dielectric constant $\epsilon(x, y)$. We assume invariance in one coordinate (\hat{z}) in keeping with the planar symmetry of most current designs. However the methodology we present can be extended to include a third dimension. In addition, our work approximates the incident laser pulse as a monochromatic plane wave at the central frequency, which is a valid approximation as long as the pulse duration is large compared to the optical period.

2.2 Adjoint Method for Particle Accelerators

Here we will discuss the use of the adjoint method to design such a structure, as explained in Ref. [1]. To begin, we must first define the optimization figure of merit and design parameters.

We first seek to maximize the *acceleration gradient* of the device, which is defined as the amount of energy gain per unit length achieved by a particle that is phased correctly with the driving field. In a general DLA device, the acceleration gradient ' G ' over a time period ' T ' is defined mathematically as

$$G = \frac{1}{T} \int_0^T E_{||}(\vec{r}(t), t) dt, \quad (2.1)$$

where $\vec{r}(t)$ is the position of the electron and $E_{||}$ signifies the (real) electric field component parallel to the electron trajectory at a given time.

Since we assume the structure is invariant in the \hat{z} direction, we may work in two dimensions, examining only the H_z , E_x and E_y field components. While this approximation neglects fringing fields that will be present in any fabricated device, it is a good approximation for the fields experienced by particles traversing the center of the acceleration channel. For an approximately monochromatic input laser source with angular frequency ω , the electric fields are, in general, of the form

$$\vec{E}(\vec{r}, t) = \Re \left\{ \tilde{E}(\vec{r}) e^{i\omega t} \right\}, \quad (2.2)$$

where \tilde{E} is complex-valued.

Let us assume the particle we wish to accelerate is moving on the line $y = 0$ with velocity $\vec{v} = \beta c_0 \hat{x}$, where c_0 is the speed of light in vacuum and $\beta \leq 1$. The x position of the particle as a function of time is given by $x(t) = x_0 + \beta c_0 t$, where x_0 represents an arbitrary choice of initial starting position. For normal incidence of the laser (laser propagating in the $+\hat{y}$ direction), phase velocity matching between the particle and the electromagnetic fields is established by introducing a spatial periodicity in our structure of period $\beta\lambda$ along \hat{x} , where λ is the laser wavelength. In the

limit of an infinitely long structure (or equivalently, $T \rightarrow \infty$) we may rewrite our expression for the gradient in Eq. (2.1) as an integral over one spatial period, given by

$$G = \frac{1}{\beta\lambda} \Re \left\{ e^{-i\phi_0} \int_0^{\beta\lambda} dx E_x(x, 0) e^{i\frac{2\pi}{\beta\lambda}x} \right\}. \quad (2.3)$$

Here the quantity $\phi_0 = \frac{2\pi x_0}{\beta\lambda}$ is representative of the phase of the particle as it enters the spatial period. In further calculations, we set $\phi_0 = 0$, only examining the acceleration gradients experienced by particles entering the accelerator with this specific phase. Since we have arbitrarily control over our input laser phase, this does not impose any constraint on the acceleration gradient attainable.

To simplify the following derivations, we define the following inner product operation involving the integral over two vector quantities \vec{a} and \vec{b} over a single period volume V'

$$\langle \vec{a}, \vec{b} \rangle = \int_{V'} dv. (\vec{a} \cdot \vec{b}) = \int_0^{\beta\lambda} dx \int_{-\infty}^{\infty} dy (\vec{a} \cdot \vec{b}). \quad (2.4)$$

With this definition, we then have the gradient

$$G = \Re \left\{ \langle \vec{E}, \vec{\eta} \rangle \right\}, \quad (2.5)$$

where we define the vector field ' $\vec{\eta}$ ' to signify the position and phase of the moving electron as

$$\vec{\eta}(x, y) = \frac{1}{\beta\lambda} e^{i\frac{2\pi}{\beta\lambda}x} \delta(y) \hat{x}. \quad (2.6)$$

The physical interpretation of $\vec{\eta}$ is diagrammed in Fig. 2.2.

Our goal in designing the accelerator for maximum acceleration gradient is to create a permittivity distribution that maximizes G subject to a few constraints. We consider performing this optimization in a small design region surrounding a small gap defined for the electron to travel through the structure. Secondly, we assume that the structure has a finite extent along the direction of the incoming laser beam. We also consider realizing this device through the patterning of a material with permittivity ϵ_{\max} . Therefore, the final device should have permittivity of either 1 or ϵ_{\max} at all points.

To perform this optimization task, we may consider discretizing our entire spatial domain into a rectangular grid, which will be necessary for numerical simulation. As our design parameters, ϕ , we take permittivity of each grid cell within the design region. Our problem then becomes finding the permittivity of each cell that will maximize the acceleration gradient, subject to each grid cell having a permittivity value of either 1 or ϵ_{\max} .

To accomplish this, the simplest approach would involve doing a direct search over the full design space. For example, one could label each cell within the design region with an identifier '0' or '1' corresponding to 'vacuum' and 'material', respectively. Then, one may generate all possible

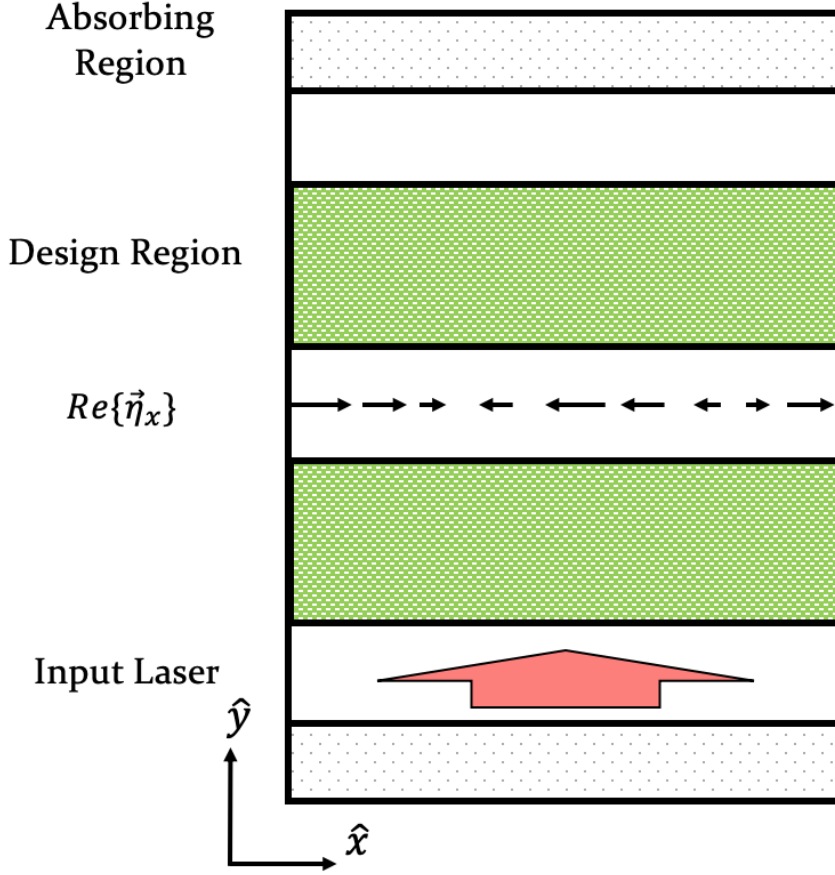


Figure 2.2: Definition of the vector field, $\vec{\eta}$, which defines the position of the electron in the frequency domain. The green regions represent domains where we will optimize the material properties using the adjoint method. The central gap is constrained to vacuum to allow passage of the electron beam. The red arrow signifies the driving laser.

structures and check their respective acceleration gradients. However, as one can imagine, this method would be far too computationally expensive to perform in practice. For example, even considering a very small design region consisting of $10 \times 10 = 100$ grid cells would result in $2^{100} \approx 10^{30}$ devices to simulate. While one may consider smart ways of searching through this device space without checking each structure, using global optimization approaches such as genetic algorithms [47] or particle swarm optimization [1], this problem is still quite computationally expensive and the size of design space becomes exponentially larger as the number of design parameters are increased.

A smarter approach involves *gradient-based optimization*, in which we search the design space according to the local gradient of the figure of merit with respect to each of the parameters. For example, we may start with an initially random device, compute how the performance will change

with respect to a change in the permittivity of each cell in the design region, and make a small update. This process may be repeated until convergence on a locally optimal solution. If the design space contains several local optima, then this whole process may be repeated several times with different initial conditions.

In fact, this method is the standard approach to training of neural networks, which may also be framed as an optimization problem over thousands to millions of parameters. We will revisit this connection in a later chapter. While the performance of gradient-based optimization is hard to directly compare to that of global optimization approaches, as the number of design parameters increases, gradient-based optimization are typically preferred as they require far fewer steps in most problems.

For gradient-based optimization to be useful, one would like an efficient means to compute the gradient of the figure of merit with respect to the design parameters. For neural networks, the gradient is computed analytically and then evaluated using the *backpropagation* algorithm [?]. For photonic devices, one may perform a similar technique using the adjoint method, which allows one to analytically compute the gradient directly from Maxwell's Equations and evaluate the result with only one additional electromagnetic simulation. This remarkable efficiency is largely responsible for the success of inverse design in photonics.

The adjoint method is typically introduced for linear optical systems, although, as we will show in a later chapter, it may be extended to nonlinear systems without much additional complication. In the frequency domain, Maxwell's equations may be written as

$$\nabla \times \nabla \times \vec{E}(\vec{r}) - k_0^2 \epsilon_r(\vec{r}) \vec{E}(\vec{r}) \equiv A\vec{E}(\vec{r}) = -i\mu_0\omega\vec{J}(\vec{r}), \quad (2.7)$$

Here, $\vec{E}(\vec{r})$ and $\vec{J}(\vec{r})$ are the electric field and electric current distributions, respectively. $k_0 = \omega/c_0$, ϵ_r is the relative permittivity and a non-magnetic material is assumed ($\mu = \mu_0$). This formalism is referred to as *finite-difference frequency-domain* (FDFD) [41, 44].

More abstractly, we may write Eq. (2.7) as

$$A\mathbf{x} = \mathbf{b}, \quad (2.8)$$

where A is a sparse, complex symmetric matrix that encodes Maxwell's equations on the device.

\mathbf{x} is a vector containing the electromagnetic fields at each position in the domain, which are the solution to Eq. (2.8) given the vector \mathbf{b} describing the electric current source distribution in the domain.

Our device is described by a set of design variables ϕ , which influence the system matrix, $A = A(\phi)$. Differentiating Eq. (2.7) with respect to ϕ , and assuming that the current source, \mathbf{b} , does

not depend on ϕ , we may recover the change in the solution with respect to the parameters as

$$\frac{d\mathbf{x}}{d\phi} = -A^{-1} \frac{\partial A}{\partial \phi} A^{-1} \mathbf{b} = -A^{-1} \frac{\partial A}{\partial \phi} \mathbf{x} \quad (2.9)$$

Now, we consider differentiating an objective function $J = J(\mathbf{x})$ that depends explicitly on the field solution. By the chain rule, this gives

$$\frac{dJ}{d\phi} = -\Re \left\{ \frac{\partial J}{\partial \mathbf{x}} \frac{d\mathbf{x}}{d\phi} \right\} = -\Re \left\{ \frac{\partial J}{\partial \mathbf{x}} A^{-1} \frac{\partial A}{\partial \phi} \mathbf{x} \right\} \quad (2.10)$$

To evaluate Eq. (2.10), we define a second simulation with source term $-\frac{\partial J}{\partial \mathbf{x}}^T$,

$$A^T \mathbf{x}_{\text{aj}} = A \mathbf{x}_{\text{aj}} = -\frac{\partial J}{\partial \mathbf{x}}^T, \quad (2.11)$$

then the field solution, $\mathbf{x}_{\text{aj}} = -A^{-1} \frac{\partial J}{\partial \mathbf{x}}^T$, can be easily identified in Eq. (2.10), which gives the expression

$$\frac{dG}{d\phi} = \Re \left\{ \mathbf{x}_{\text{aj}}^T \frac{\partial A}{\partial \phi} \mathbf{x} \right\}. \quad (2.12)$$

The only quantity in this expression that depends on the parameter ϕ is $\frac{\partial A}{\partial \phi}$. As we will soon discuss, this quantity will generally be trivial to compute. On the other hand, the full field calculations of \mathbf{x} and \mathbf{x}_{aj} are computationally expensive, but may be computed once and used for an arbitrarily large set of parameters ϕ_i . This gives the adjoint method significant scaling advantage with respect to traditional direct sensitivity methods, such as finite difference, which require a separate full-field calculation for each parameter being investigated.

Previously, we expressed the acceleration gradient as the inner product of the electric fields $\vec{E}(\vec{r})$ and our vector field $\vec{\eta}(\vec{r})$ as

$$G = \Re \left\{ \langle \vec{E}, \vec{\eta} \rangle \right\}, \quad (2.13)$$

which we may express in matrix notation as

$$G = \Re \left\{ \boldsymbol{\eta}^T \mathbf{x} \right\}, \quad (2.14)$$

where $\boldsymbol{\eta}$ is a vector representing $\vec{\eta}$ on the finite difference grid and \mathbf{x} is a vector containing the electric fields, as before.

In this notation, the adjoint problem is therefore

$$A^T \mathbf{x}_{\text{aj}} = -\frac{\partial G}{\partial \mathbf{x}}^T = -\boldsymbol{\eta}. \quad (2.15)$$

Intuitively, this represents a situation where the electric current source is located at the central

gap where the accelerator is traversing the structure. To make this point more explicit, let us now consider the fields radiated by a point particle of charge q flowing through our domain at $y = 0$ with velocity $\vec{v} = \beta c_0 \hat{x}$. In the time domain, we can represent the current density of this particle as

$$\vec{J}_{\text{rad}}(x, y; t) = q\beta c_0 \delta(x - x_0 - c_0 \beta t) \delta(y) \hat{x}. \quad (2.16)$$

To express this in the frequency domain, we take the Fourier transform of \vec{J}_{rad} with respect to time, giving

$$\begin{aligned} \vec{J}_{\text{rad}}(x, y; \omega) &= q\beta c_0 \delta(y) \hat{x} \int_{-\infty}^{\infty} dt \exp(-i\omega t) \delta(x - x_0 - c_0 \beta t) \\ &= q \exp\left(i \frac{\omega (x - x_0)}{c_0 \beta}\right) \delta(y) \hat{x} \\ &= q \exp\left(i \frac{2\pi}{\beta \lambda} x\right) \exp(-i\phi_0) \delta(y) \hat{x}. \end{aligned} \quad (2.17)$$

Comparing with the source of our adjoint problem, $\vec{J}_{\text{aj}} = \frac{-i}{\omega \mu_0} \vec{\eta}$, we can see that

$$\vec{J}_{\text{aj}} = \frac{-i \exp(i\phi_0)}{2\pi q \beta c_0 \mu_0} \vec{J}_{\text{rad}}. \quad (2.18)$$

This finding shows that the adjoint field solution (\vec{E}_{aj}) corresponds (up to a complex constant) to the field radiating from a test particle flowing through the accelerator structure. To put this another way, in order to calculate the acceleration gradient sensitivity with the adjoint problem, we must simulate the same structure operating both as an accelerator ($\vec{E} = -i\omega \mu_0 \vec{J}_{\text{acc}}$) and as a radiator ($A \vec{E}_{\text{aj}} = -i\omega \mu_0 \vec{J}_{\text{aj}}$).

It is understood that one way to create acceleration is to run a radiative process in reverse. Indeed, this is the working principle behind accelerator schemes such as inverse free electron lasers [32, 11], inverse Cherenkov accelerators [22, 15], and inverse Smith-Purcell accelerators [5, 30]. Here, we see that this relationship can be expressed in an elegant fashion using the adjoint method.

We now confirm that the adjoint gradient matches the results obtained by direct sensitivity analysis, we examine a simple accelerator geometry composed of two opposing dielectric squares each of relative permittivity ϵ . We take a single ϕ parameter to be the relative permittivity of the entire square region. Because we only change the region inside the dielectric square, we may identify the $\frac{\partial A}{\partial \phi}$ operator from Eq. (2.7) as

$$\frac{dA}{d\epsilon}(\vec{r}) = \begin{cases} -k_0^2 & \text{if } \vec{r} \text{ in square} \\ 0 & \text{otherwise} \end{cases}. \quad (2.19)$$

Thus, given the form of the sensitivity of the acceleration gradient from Eq. (2.12), combined with Eq. (2.19), the change in acceleration gradient with respect to changing the entire square permittivity is simply given by the integral of the two field solutions over the square region, labeled

‘ sq ’

$$\frac{dG}{d\epsilon_{sq}} = -k_0^2 \Re \left\{ \int_{sq} d^2\vec{r} \cdot \vec{E}(\vec{r}) \cdot \vec{E}_{aj}(\vec{r}) \right\}. \quad (2.20)$$

In Fig. Fig. 2.3 we compare this result with the direct sensitivity calculation where the system is manually changed and simulated again, using a finite difference derivative. The two methods agree with excellent precision, which confirms that the adjoint formalism is giving the correct results.

Extending this example to the general case of perturbing the permittivity at an arbitrary position \vec{r} , we see that

$$\begin{aligned} \frac{dG}{d\epsilon}(\vec{r}) &= -k_0^2 \Re \left\{ \int d^2\vec{r}' \cdot \vec{E}(\vec{r}') \cdot \vec{E}_{aj}(\vec{r}') \cdot \delta(\vec{r} - \vec{r}') \right\} \\ &= -k_0^2 \Re \left\{ \vec{E}(\vec{r}) \cdot \vec{E}_{aj}(\vec{r}) \right\}. \end{aligned} \quad (2.21)$$

2.3 Inverse design of Dielectric Laser Accelerator

With the mathematical form of the adjoint problem discussed, now we focus on the optimization and inverse design of the DLA device. In our FDFD simulation, we use a grid spacing that corresponds to 200 grid points per free space wavelength in each dimension. Perfectly matched layers are implemented as absorbing regions on the edges parallel to the electron trajectory, with periodic boundary conditions employed on boundaries perpendicular to the electron trajectory. A total-field scattered-field [44] formalism is used to create a perfect plane wave input for the acceleration mode.

Since the adjoint method gives us a highly efficient method to calculate $\frac{dG}{d\epsilon_i}$, we use this information in an iterative optimization procedure. During each iteration, we first calculate $\frac{dG}{d\epsilon_i}$ for all pixels ‘ i ’ within some specified design region. Then, we update the ϵ_i of each grid cell as follows

$$\epsilon_i := \epsilon_i + \alpha \frac{dG}{d\epsilon_i}. \quad (2.22)$$

Here, α is a step parameter that we can tune. We need α to be small enough to find local maxima, but large enough to have the optimization run in reasonable amount of time. This process is repeated until convergence on G , as diagrammed in Fig. 2.4.

During the course of optimization, the permittivity distribution is considered as a continuous variable, which is not realistic in physical devices. To address this issue, we employ a permittivity capping scheme during optimization. We define a maximum permittivity ‘ ϵ_m ’ corresponding to a material of interest. During the iterative process, if the relative permittivity of any cell becomes either less than 1 (vacuum) or greater than ϵ_m , that cell is pushed back into the acceptable range. It was found that with this capping scheme, the structures converged to binary (each pixel being either vacuum or material with a permittivity of ϵ_m) after a number of iterations without specifying this choice of binary materials as a requirement of the optimization. Therefore, only minimal post-processing of the structures was required. Since high index contrast is favorable for maximizing the

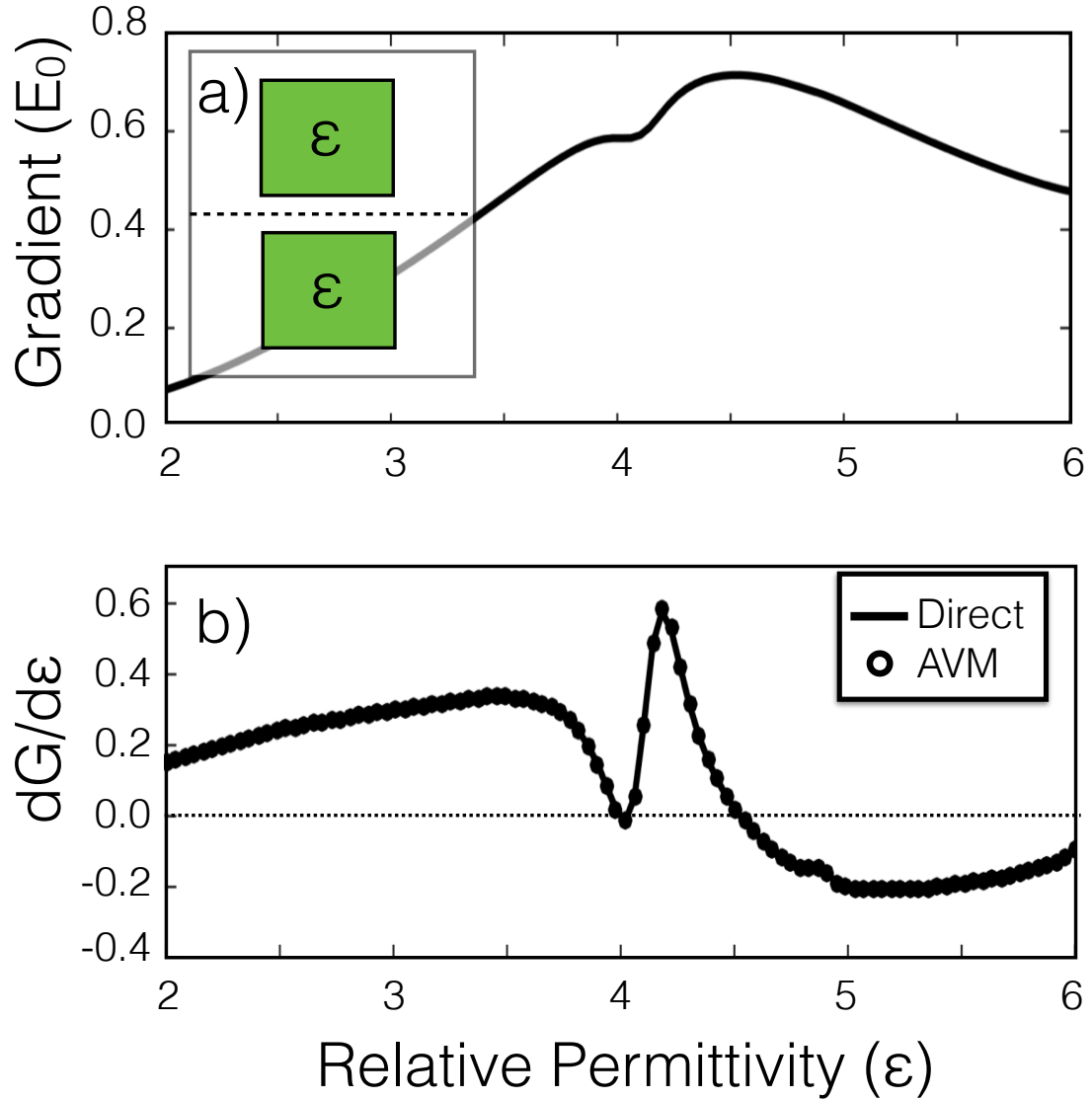


Figure 2.3: Demonstration of adjoint method in calculating accelerator sensitivities. (a) The acceleration gradient (G) of a square accelerator structure (inset) as a function of the square's relative permittivity. We express the acceleration gradient in its dimensionless form, normalized by the electric field amplitude of the incident plane wave (E_0). The particle traverses along the dotted line with a velocity of c_0 ($\beta = 1$) and a plane wave is incident from the bottom of the structure. (b) The sensitivity $\frac{dG}{d\epsilon}$ of the gradient with respect to changing the square relative permittivity for direct central difference (solid line) $\frac{dG}{d\epsilon} = \frac{G(\epsilon+\Delta\epsilon) - G(\epsilon-\Delta\epsilon)}{2\Delta\epsilon}$ and using the adjoint method (circles). The two calculations agree with excellent precision. The dotted line at $\frac{dG}{d\epsilon} = 0$, corresponds to local minima and maxima of $G(\epsilon)$ above.

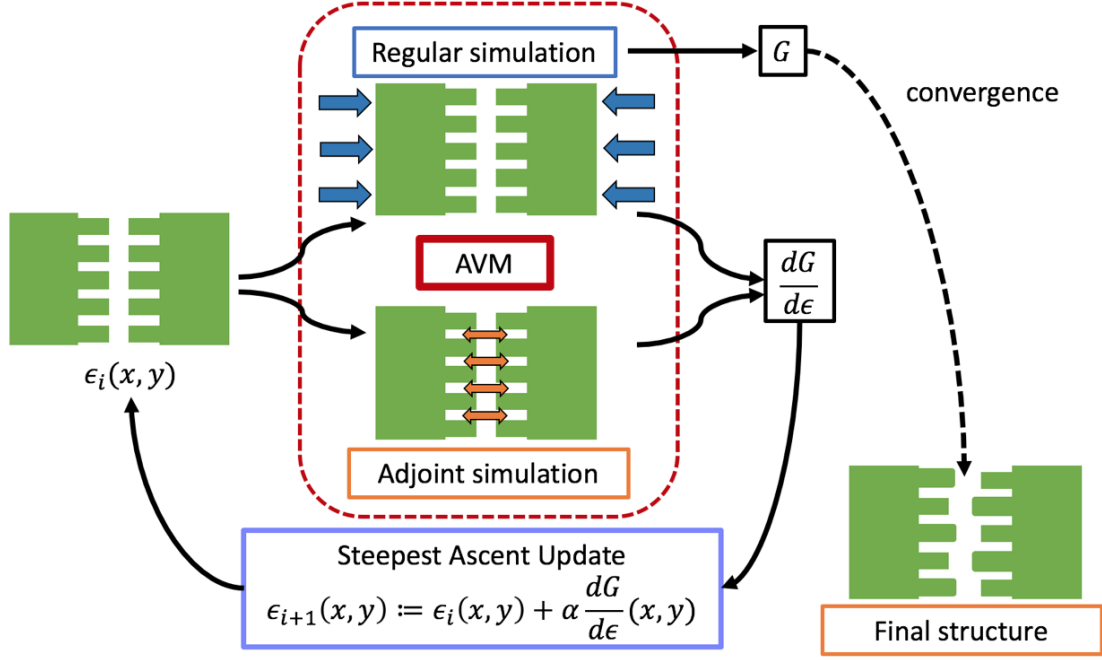


Figure 2.4: Optimization routine for DLA.

acceleration gradient, the optimization often favors increasing index contrast within the structure, which leads to each pixel being pushed towards either 1 or ϵ_m . This is a possible explanation for why the structures converge to binary distributions under our optimization procedure.

The results of this optimization scheme are shown in Figs. 2.5(b)-2.5(d) for three different ϵ_m values corresponding to commonly explored DLA materials. The design region was taken to be a rectangle fully surrounding but not including the particle gap. The design region was made smaller for higher index materials, since making it too large led to divergence during the iteration. We found that a totally vacuum initial structure worked well for these optimizations. However, initially random values between 1 and ϵ_m for each pixel within the design region also gave reasonable results. For materials of Si, Si_3N_4 , and SiO_2 , the achieved gradients (normalized by the incident field, E_0) were 0.90, 0.56, and 0.31 (E_0), respectively. Assuming incident field values consistent with the laser damage thresholds given in Ref. [43], these correspond to acceleration gradients of 0.25, 0.83, and 1.33 GV m^{-1} , respectively. Without the dielectric mirrors, these structures give normalized acceleration gradients of 0.28, 0.15, and 0.07 (E_0), respectively. For comparison, the Si dual pillar structures presented in Ref. [26] give gradients of around 0.3 (E_0). Therefore, the adjoint optimized structures show about a three-fold improvement in acceleration gradient over established structures.

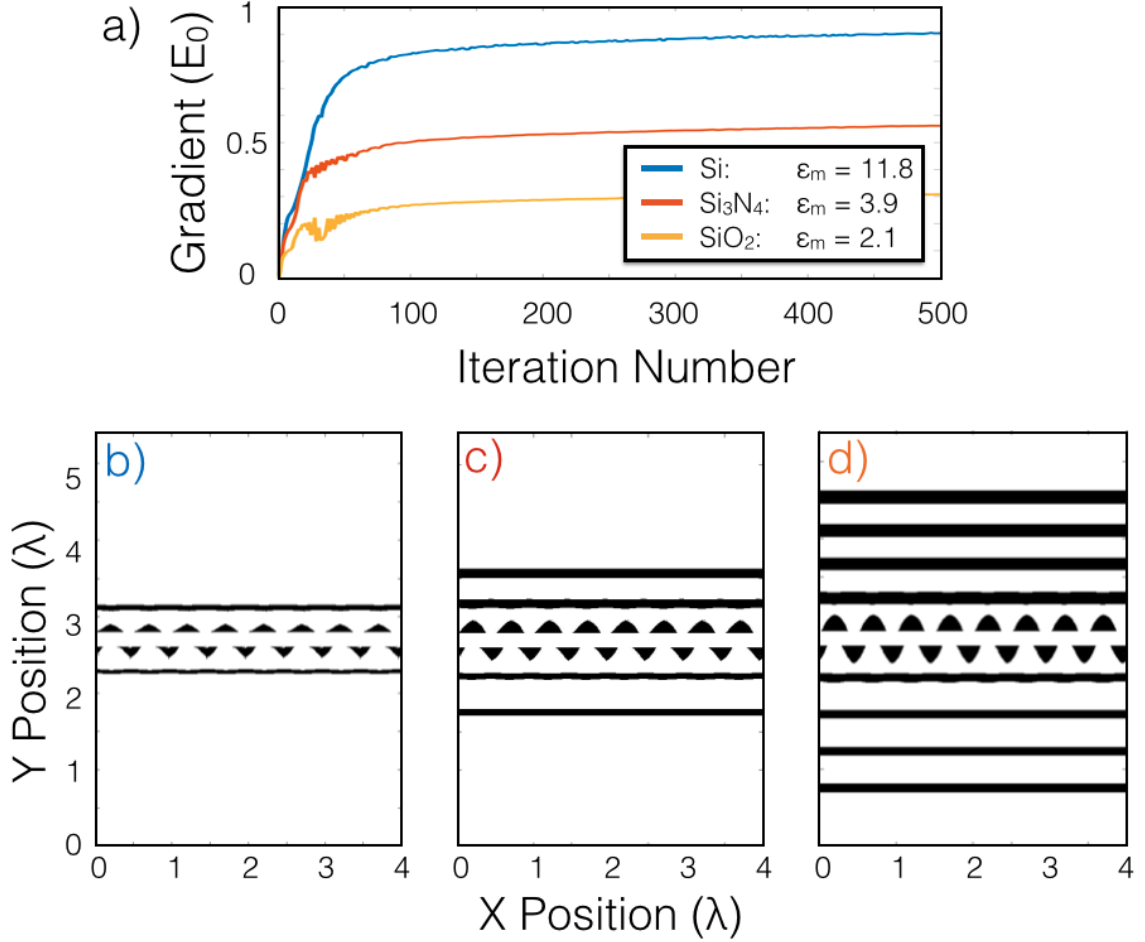


Figure 2.5: Demonstration of the structure optimization for $\beta = 0.5$, laser wavelength $\lambda = 2 \mu\text{m}$, and a gap size of 400 nm. A plane wave is incident from the bottom in all cases. (a) Acceleration gradient as a function of iteration number for different maximum relative permittivity values, corresponding to those of Si, Si_3N_4 , and SiO_2 at the laser wavelength. The acceleration gradient is normalized by the electric field amplitude of the incident plane wave (E_0). The optimizations converge after about five-hundred iterations. (b-d) Final structure permittivity distributions (white = vacuum, black = ϵ_m) corresponding to the three curves in (a). Eight periods are shown, corresponding to four laser wavelengths. For each (b-d), design region widths on each side of the particle gap were given by 1, 2, and $4 \mu\text{m}$ for Si, Si_3N_4 , and SiO_2 , respectively.

This optimization scheme seems to favor geometries consisting of a staggered array of field-reversing pillars surrounding the vacuum gap, which is already a popular geometry for DLA. However, these optimal designs also include reflective mirrors on either side of the pillar array, which suggests that for strictly higher acceleration gradients, it is useful to use dielectric mirrors to resonantly enhance the fields in the gap.

It was observed that for random initial starting permittivity distributions, the same structures as shown in Fig. 2.5 are generated every time. Furthermore, as shown in Fig. 2.6, the geometries found using this method are remarkably similar to those recently proposed through human design using physical intuition [25]. These findings together suggest that the proposed structures may be close to the globally optimal structure for maximizing G .

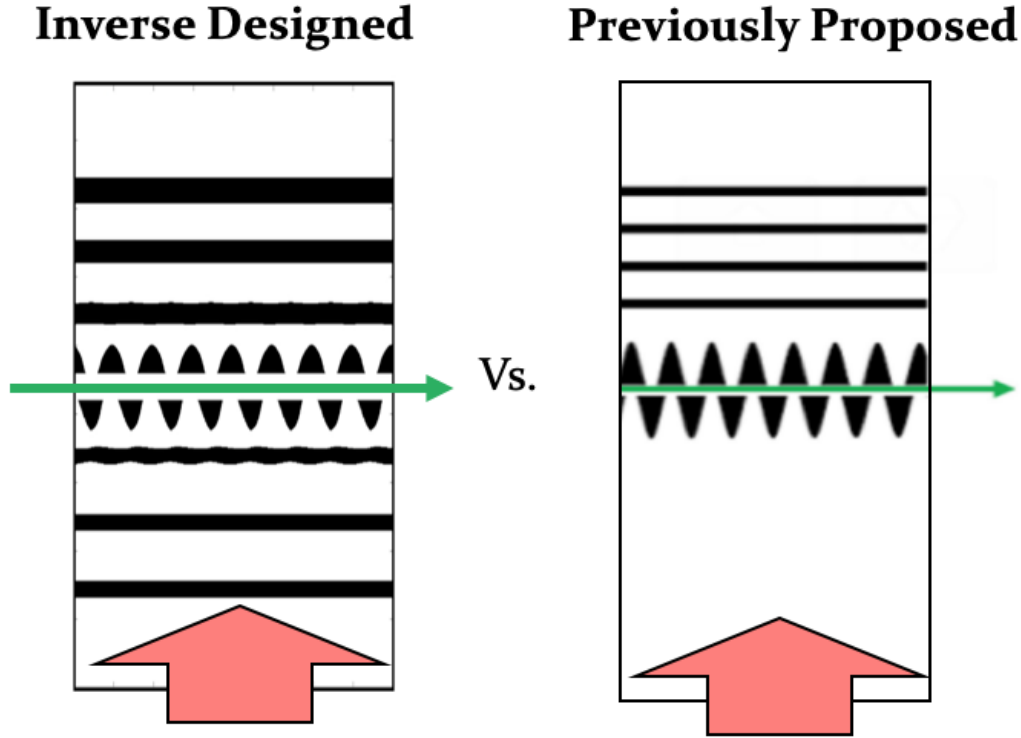


Figure 2.6: Similarity between DLA structures designed using adjoint method (left) and those independently proposed using human intuition.

It was further found that convergence could be achieved faster by a factor of about ten by including a ‘momentum’ term in the update equation. This term corresponds to the sensitivity calculated at the last iteration multiplied by a constant, $\alpha' < 1$. Explicitly, for iteration number ‘ j ’ and pixel ‘ i ’

$$\epsilon_i^{(j+1)} := \epsilon_i^{(j)} + \alpha \left[\frac{dG^{(j)}}{d\epsilon_i} + \alpha' \frac{dG^{(j-1)}}{d\epsilon_i} \right]. \quad (2.23)$$

2.4 Optimization of acceleration factor

DLAs are often driven with the highest input field possible before damage occurs. Therefore, another highly relevant quantity to maximize is the *acceleration factor*, given by the acceleration gradient divided by the maximum electric field amplitude in the system. This quantity will ultimately limit the amount of acceleration gradient we can achieve when running at damage threshold. Explicitly, the acceleration factor is given by

$$f_A = \frac{G}{\max\{|\vec{E}|\}}. \quad (2.24)$$

Here, $|\vec{E}|$ is a vector of electric field amplitudes in our system, which are normalized, as in the case of G , by the electric field amplitude of the incident plane wave (E_0). The $\max\{\}$ function is designed to pick out the highest value of this vector in either our design or material region, depending on the context. The *design region* is defined as the total region outside of the particle gap where the permittivity is updated. The *material region* is defined as any region where the permittivity is equal to ϵ_m . We would like to use the same basic formalism to maximize f_A . However, since the $\max\{\}$ function is not differentiable, this is not possible directly. Instead we may use a ‘smooth-max’ function to approximate $\max\{\}$ as a weighted sum of vector components

$$\max\{|\vec{E}|\} \approx \frac{\sum_i |\vec{E}_i| \exp(a|\vec{E}_i|)}{\sum_i \exp(a|\vec{E}_i|)}. \quad (2.25)$$

Here, the parameter $a \geq 0$ controls the relative strength of the exponential sum terms, for $a = 0$, this function simply gives the average value of the field amplitudes. By sweeping a and examining the acceleration factors of the resulting optimized structures, we determined that $a = 3$ gave the best improvement in f_A . If a is too large, the calculation may induce floating point overflow or rounding error issues.

Using this smooth-max function, one may calculate $\frac{df_A}{d\epsilon_i}$ analytically and perform structure optimizations in the same way that was discussed previously. The derivation of the adjoint source term is especially complicated and omitted for brevity, although the end result is expressed solely in terms of the original fields, the adjoint fields, and the $\frac{d}{d\gamma}$ operator, as before. Two structures with identical parameters but optimized, respectively, for maximum G and f_A are shown in Fig. 2.7. On the left, we see that the G maximized structure shows the characteristic dielectric mirrors, giving resonant field enhancement. On the right is the structure optimized for f_A , which has eliminated most of its dielectric mirrors and also introduces interesting pillar shapes. In Table 2.1 the main DLA performance quantities of interest are compared between these two structures. Whereas the acceleration gradient is greatly reduced when maximizing for f_A , the f_A value itself is improved by about 25% or 23% depending on whether one measures the maximum field in the design region or the material region, respectively. As a comparison with the geometry from Ref. [26], a SiO₂ dual

pillar structure with a 400 nm gap was optimized for acceleration gradient, giving an acceleration gradient of 0.025 (E_0) with a pillar radius of 670 nm. This structure was found to have $\max\{|\vec{E}|\}$ in the design region of 1.612 (E_0) and $\max\{|\vec{E}|\}$ in the material region of 1.209 (E_0), leading to acceleration factors of 0.016 and 0.021, respectively. Comparing these numbers to those in Table 2.1, it is apparent that the AVM-optimized structures perform better than the dual pillar structures in terms of both gradient and acceleration factor.

These findings suggest that the inverse design strategy is effective in designing not only resonant, high acceleration gradient structures, but also non-resonant structures that are more damage resistant. In the future, when more components of DLA are moved on-chip (such as the optical power delivery), it will be important to have control over the resonance characteristics of the DLA structures to prevent damage breakdown at the input facet. Our technique may be invaluable in designing structures with tailor-made quality factors for this application.

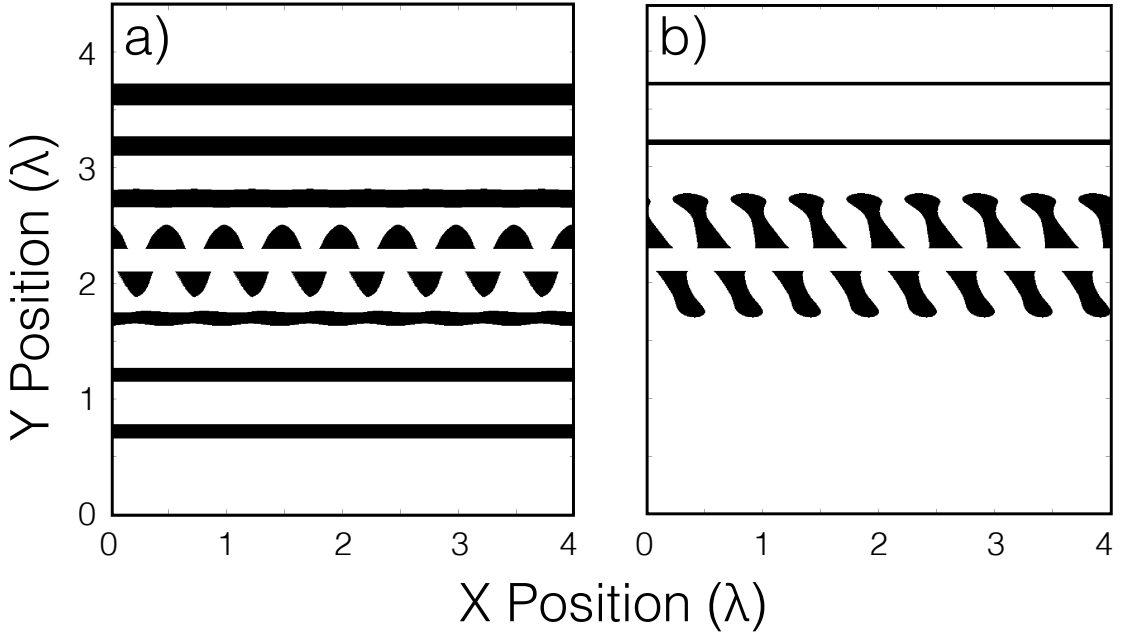


Figure 2.7: Demonstration of the final structures after optimization for (a) maximizing gradient only, (b) maximizing the acceleration factor. $\beta = 0.5$, laser wavelength $\lambda = 2 \mu\text{m}$, gap size of 400 nm. $\epsilon_m = 2.1$, corresponding to SiO_2 . In (a), the high gradients are achieved using reflective dielectric mirrors to confine and enhance the fields in the center region. In (b), these dielectric mirrors are removed and the pillar structures are augmented. The structure in (b) shows a 23% increase in the acceleration factor in the material region when compared to (a).

Table 2.1: Acceleration factor (f_A) before and after maximization.

Quantity	Value (max G)	Value (max f_A)	Chang.
Gradient (E_0)	0.1774	0.0970	-45.32%
$\max\{ \vec{E} \}$ in design region (E_0)	4.1263	1.7940	-56.52%
$\max\{ \vec{E} \}$ in material region (E_0)	2.7923	1.2385	-55.84%
f_A in design region	0.0430	0.0541	+25.81%
f_A in material region	0.0635	0.0783	+23.31%

2.5 Conclusions

We found that the adjoint method is a reliable method for optimizing DLA structures for both maximum acceleration gradient and also acceleration factor. The optimization algorithm discussed shows good convergence and rarely requires further post-processing of structures to create binary permittivity distributions. Therefore, it is a simple and effective method for designing DLAs. Whereas most structure optimization in this field uses parameter sweeps to search the design space, the efficiency of our method allows us to more intelligently find optimal geometries without shape parameterization. Furthermore, the structures that we design are fabricable.

Although no DLA structures have been tested at the proposed wavelength of $2\mu\text{m}$, both simulations [38] and experimental results from other wavelengths [26] show gradients far below those presented here. We had limited success designing DLA structures in the relativistic ($\beta \approx 1$) regime, especially for higher index materials, such as Si. We believe this is largely due to the stronger coupling between electron beam and incident plane wave at this energy. The characteristics of the adjoint source change dramatically at the $\beta = 1$ point. Whereas in the sub-relativistic regime, the adjoint source generates an evanescent near-field extending from the gap particle position, at $\beta \geq 1$, the adjoint fields become propagating by process of Cherenkov radiation. Upon using the above described algorithm, the gradients diverge before returning to low values, no matter the step size α . The only way to mitigate this problem is to choose prohibitively small design regions or low index materials, such as SiO_2 .

In addition to the side-incident geometry explored, this technique is applicable to designing other dielectric-based accelerator structures. This includes particle-laser co-propagating schemes [12] and dielectric wakefield acceleration [49], among others. Therefore, we expect that our results may find use in the larger advanced accelerator community.

In this chapter, we have introduced the adjoint variable method as a powerful tool for designing dielectric laser accelerators for high gradient acceleration and high acceleration factor. We have further shown that the adjoint simulation is sourced by a point charge flowing through the accelerator, which quantifies the reciprocal relationship between an accelerator and a radiator.

Optimization algorithms built on this approach allow us to search a substantially larger design space and generate structures that give acceleration gradients far above those normally used for

each material. Furthermore, the structures designed by adjoint are fundamentally not constrained by shape parameterization, allowing never-before-seen geometries to be generated and tested. This theme will continue to be explored in other chapters.

Chapter 3

Integrated Photonic Circuit for Accelerators on a Chip

3.1 Motivation

3.2 On-Chip Laser Coupling Device

3.3 Parameter Study

3.4 Automatic Controlled Power Delivery Systems

3.4.1 Phase Control Mechanism

3.4.2 Power Control Mechanism using Reconfigurable Circuit

Deterministic Tuning Algorithm

Scaling Gains

3.5 Experimental Efforts

3.5.1 Waveguide Damage and Nonlinearity Measurements

3.5.2 Demonstration of Waveguide-Coupled Acceleration

Chapter 4

Training of Optical Neural Networks

4.1 Introduction to Machine Learning

4.1.1 Applications

4.1.2 Hardware Demands

4.2 Linear Nanophotonic Processors

4.3 Optical Neural Networks

4.3.1 Conventional Neural Network

4.3.2 Optical Integration

4.3.3 Training Protocols

Computer Model Training

Brute Force Training

4.4 In Situ Backpropagation Training

4.4.1 Derivation Using Adjoint Method

4.4.2 Method for Measurement of Adjoint Gradient

4.4.3 Numerical Demonstrations

4.5 Electro-Optic Activation Functions

4.5.1 Motivation

4.5.2 Research Activation Functions

Chapter 5

Extension of Adjoint Method beyond Linear Time-Invariant Systems.

5.1 Nonlinear Devices

5.1.1 Generalization of Adjoint Method to Nonlinear Problems

5.1.2 Inverse Design of Nonlinear Photonic Switches

5.2 Active Devices

5.2.1 Adjoint Sensitivity for Multi-Frequency FDTD Problems

5.2.2 Inverse Design of Optical Isolators through Dynamic Modulation

5.3 Adjoint for Time Domain

5.3.1 Derivation

5.3.2 Challenges

5.4 Forward-mode Differentiation

Chapter 6

Conclusion and Final Remarks

Appendix A

Something

Some appendix section.

Bibliography

- [1] Particle swarm optimization: developments, applications and resources - IEEE Conference Publication.
- [2] Govind P. Agrawal. *Fiber-Optic Communication Systems*. John Wiley & Sons, February 2012.
- [3] Selcuk Akturk et al. Pulse-front tilt caused by spatial and temporal chirp. *Opt. Express*, 12(19):4399–4410, 2004.
- [4] Mordecai Avriel. *Nonlinear programming: analysis and methods*. Courier Corporation, 2003.
- [5] J Bae et al. Experimental verification of the theory on the inverse Smith–Purcell effect at a submillimeter wavelength. *Appl. Phys. Lett.*, 61(7):870–872, 1992.
- [6] P. I. Borel, A. Harpøth, L. H. Frandsen, M. Kristensen, P. Shi, J. S. Jensen, and O. Sigmund. Topology optimization and fabrication of photonic crystal structures. *Optics Express*, 12(9):1996–2001, May 2004.
- [7] John Breuer et al. Dielectric laser acceleration of electrons in the vicinity of single and double grating structures-theory and simulations. *J. Phys. B: At. Mol. Opt. Phys.*, 47(23):234004, 2014.
- [8] John Breuer et al. Dielectric laser acceleration of nonrelativistic electrons at a single fused silica grating structure: Experimental part. *Phys. Rev. ST Accel. Beams*, 17(2):021301, 2014.
- [9] D. E. Carlson and C. R. Wronski. Amorphous silicon solar cell. *Applied Physics Letters*, 28(11):671–673, June 1976.
- [10] Chia-Ming Chang and Olav Solgaard. Silicon buried gratings for dielectric laser electron accelerators. *Appl. Phys. Lett.*, 104(18):184102, 2014.
- [11] E. D. Courant et al. High-energy inverse free-electron laser accelerator. *AIP Conf. Proc.*, 127(1):849–874, 1985.

- [12] Benjamin M Cowan. Three-dimensional dielectric photonic crystal structures for laser-driven acceleration. *Phys. Rev. ST Accel. and Beams*, 11(1):011301, 2008.
- [13] Jay W Dawson et al. Analysis of the scalability of diffraction-limited fiber lasers and amplifiers to high average power. *Opt. Express*, 16(17):13240–13266, 2008.
- [14] R Joel England et al. Dielectric laser accelerators. *Rev. Mod. Phys.*, 86(4):1337, 2014.
- [15] J R Fontana and R H Pantell. A high-energy, laser accelerator for electrons using the inverse Cherenkov effect. *J. Appl. Phys.*, 54(8):4285–4288, 1983.
- [16] J Hebling. Derivation of the pulse front tilt caused by angular dispersion. *Opt. Quant. Electron.*, 28(12):1759–1763, 1996.
- [17] Po-Chun Hsu, Alex Y. Song, Peter B. Catrysse, Chong Liu, Yucan Peng, Jin Xie, Shanhui Fan, and Yi Cui. Radiative human body cooling by nanoporous polyethylene textile. *Science*, 353(6303):1019–1023, September 2016.
- [18] B. Jalali and S. Fathpour. Silicon Photonics. *Journal of Lightwave Technology*, 24(12):4600–4615, December 2006.
- [19] Antony Jameson. Aerodynamic Shape Optimization Using the Adjoint Method. page 30.
- [20] J. S. Jensen, O. Sigmund, L. H. Frandsen, P. I. Borel, A. Harpoth, and M. Kristensen. Topology design and fabrication of an efficient double 90/spl deg/ photonic Crystal waveguide bend. *IEEE Photonics Technology Letters*, 17(6):1202–1204, June 2005.
- [21] Jan Kern, Ruchira Chatterjee, Iris D. Young, Franklin D. Fuller, Louise Lassalle, Mohamed Ibrahim, Sheraz Gul, Thomas Fransson, Aaron S. Brewster, Roberto Alonso-Mori, Rana Hussein, Miao Zhang, Lacey Douthit, Casper de Lichtenberg, Mun Hon Cheah, Dmitry Shevela, Julia Wersig, Ina Seuffert, Dimosthenis Sokaras, Ernest Pastor, Clemens Weninger, Thomas Kroll, Raymond G. Sierra, Pierre Aller, Agata Butryn, Allen M. Orville, Mengning Liang, Alexander Batyuk, Jason E. Koglin, Sergio Carbajo, Sébastien Boutet, Nigel W. Moriarty, James M. Holton, Holger Dobbek, Paul D. Adams, Uwe Bergmann, Nicholas K. Sauter, Athina Zouni, Johannes Messinger, Junko Yano, and Vittal K. Yachandra. Structures of the intermediates of Kok’s photosynthetic water oxidation clock. *Nature*, 563(7731):421, November 2018.
- [22] W D Kimura et al. Laser acceleration of relativistic electrons using the inverse Cherenkov effect. *Phys. Rev. Lett.*, 74(4):546, 1995.
- [23] Diederik P. Kingma and Jimmy Ba. Adam: A Method for Stochastic Optimization. *arXiv:1412.6980 [cs]*, December 2014. arXiv: 1412.6980.

- [24] M Kozák et al. Dielectric laser acceleration of sub-relativistic electrons by few-cycle laser pulses. *Nucl. Instrum. Methods Phys. Res., Sect. A*, 2016. DOI: 10.1016/j.nima.2016.12.051.
- [25] Martin Kozak. Status report erlangen (hommelhoff group). ACHIP 3rd Collaboration Meeting, 2016.
- [26] Kenneth J Leedle et al. Dielectric laser acceleration of sub-100 keV electrons with silicon dual-pillar grating structures. *Opt. Lett.*, 40(18):4344–4347, 2015.
- [27] LIGO Scientific Collaboration and Virgo Collaboration, B. P. Abbott, R. Abbott, T. D. Abbott, M. R. Abernathy, F. Acernese, K. Ackley, C. Adams, T. Adams, P. Addesso, R. X. Adhikari, V. B. Adya, C. Affeldt, M. Agathos, K. Agatsuma, N. Aggarwal, O. D. Aguiar, L. Aiello, A. Ain, P. Ajith, B. Allen, A. Allocca, P. A. Altin, S. B. Anderson, W. G. Anderson, K. Arai, M. A. Arain, M. C. Araya, C. C. Arceneaux, J. S. Areeda, N. Arnaud, K. G. Arun, S. Ascenzi, G. Ashton, M. Ast, S. M. Aston, P. Astone, P. Aufmuth, C. Aulbert, S. Babak, P. Bacon, M. K. M. Bader, P. T. Baker, F. Baldaccini, G. Ballardín, S. W. Ballmer, J. C. Barayoga, S. E. Barclay, B. C. Barish, D. Barker, F. Barone, B. Barr, L. Barsotti, M. Barsuglia, D. Barta, J. Bartlett, M. A. Barton, I. Bartos, R. Bassiri, A. Basti, J. C. Batch, C. Baune, V. Bavigadda, M. Bazzan, B. Behnke, M. Bejger, C. Belczynski, A. S. Bell, C. J. Bell, B. K. Berger, J. Bergman, G. Bergmann, C. P. L. Berry, D. Bersanetti, A. Bertolini, J. Betzwieser, S. Bhagwat, R. Bhandare, I. A. Bilenko, G. Billingsley, J. Birch, R. Birney, O. Birnholtz, S. Biscans, A. Bisht, M. Bitossi, C. Biwer, M. A. Bizouard, J. K. Blackburn, C. D. Blair, D. G. Blair, R. M. Blair, S. Bloemen, O. Bock, T. P. Bodiya, M. Boer, G. Bogaert, C. Bogan, A. Bohe, P. Bojtos, C. Bond, F. Bondu, R. Bonnand, B. A. Boom, R. Bork, V. Boschi, S. Bose, Y. Bouffanais, A. Bozzi, C. Bradaschia, P. R. Brady, V. B. Braginsky, M. Branchesi, J. E. Brau, T. Briant, A. Brillet, M. Brinkmann, V. Brisson, P. Brockill, A. F. Brooks, D. A. Brown, D. D. Brown, N. M. Brown, C. C. Buchanan, A. Buikema, T. Bulik, H. J. Bulten, A. Buonanno, D. Buskulic, C. Buy, R. L. Byer, M. Cabero, L. Cadonati, G. Cagnoli, C. Cahillane, J. Calderón Bustillo, T. Callister, E. Calloni, J. B. Camp, K. C. Cannon, J. Cao, C. D. Capano, E. Capocasa, F. Carbognani, S. Caride, J. Casanueva Diaz, C. Casentini, S. Caudill, M. Cavaglià, F. Cavalier, R. Cavalieri, G. Cella, C. B. Cepeda, L. Cerboni Baiardi, G. Cerretani, E. Cesarini, R. Chakraborty, T. Chalermongsak, S. J. Chamberlin, M. Chan, S. Chao, P. Charlton, E. Chassande-Mottin, H. Y. Chen, Y. Chen, C. Cheng, A. Chincarini, A. Chiummo, H. S. Cho, M. Cho, J. H. Chow, N. Christensen, Q. Chu, S. Chua, S. Chung, G. Ciani, F. Clara, J. A. Clark, F. Cleva, E. Coccia, P.-F. Cohadon, A. Colla, C. G. Collette, L. Cominsky, M. Constancio, A. Conte, L. Conti, D. Cook, T. R. Corbitt, N. Cornish, A. Corsi, S. Cortese, C. A. Costa, M. W. Coughlin, S. B. Coughlin, J.-P. Coulon, S. T. Countryman, P. Couvares, E. E. Cowan, D. M. Coward, M. J. Cowart, D. C. Coyne, R. Coyne, K. Craig, J. D. E. Creighton, T. D. Creighton, J. Cripe, S. G.

Crowder, A. M. Cruise, A. Cumming, L. Cunningham, E. Cuoco, T. Dal Canton, S. L. Danilishin, S. D’Antonio, K. Danzmann, N. S. Darman, C. F. Da Silva Costa, V. Dattilo, I. Dave, H. P. Daveloza, M. Davier, G. S. Davies, E. J. Daw, R. Day, S. De, D. DeBra, G. Debreczeni, J. Degallaix, M. De Laurentis, S. Deléglise, W. Del Pozzo, T. Denker, T. Dent, H. Dereli, V. Dergachev, R. T. DeRosa, R. De Rosa, R. DeSalvo, S. Dhurandhar, M. C. Díaz, L. Di Fiore, M. Di Giovanni, A. Di Lieto, S. Di Pace, I. Di Palma, A. Di Virgilio, G. Dojcinoski, V. Dolique, F. Donovan, K. L. Dooley, S. Doravari, R. Douglas, T. P. Downes, M. Drago, R. W. P. Dr-ever, J. C. Driggers, Z. Du, M. Ducrot, S. E. Dwyer, T. B. Edo, M. C. Edwards, A. Effler, H.-B. Eggenstein, P. Ehrens, J. Eichholz, S. S. Eikenberry, W. Engels, R. C. Essick, T. Etzel, M. Evans, T. M. Evans, R. Everett, M. Factourovich, V. Fafone, H. Fair, S. Fairhurst, X. Fan, Q. Fang, S. Farinon, B. Farr, W. M. Farr, M. Favata, M. Fays, H. Fehrmann, M. M. Fejer, D. Feldbaum, I. Ferrante, E. C. Ferreira, F. Ferrini, F. Fidecaro, L. S. Finn, I. Fiori, D. Fiorucci, R. P. Fisher, R. Flaminio, M. Fletcher, H. Fong, J.-D. Fournier, S. Franco, S. Frasca, F. Frasconi, M. Frede, Z. Frei, A. Freise, R. Frey, V. Frey, T. T. Fricke, P. Fritschel, V. V. Frolov, P. Fulda, M. Fyffe, H. A. G. Gabbard, J. R. Gair, L. Gammaitoni, S. G. Gaonkar, F. Garufi, A. Gatto, G. Gaur, N. Gehrels, G. Gemme, B. Gendre, E. Genin, A. Gennai, J. George, L. Gergely, V. Germain, Abhirup Ghosh, Archisman Ghosh, S. Ghosh, J. A. Giaime, K. D. Giardina, A. Giazotto, K. Gill, A. Glaefke, J. R. Gleason, E. Goetz, R. Goetz, L. Gondan, G. González, J. M. Gonzalez Cas-tro, A. Gopakumar, N. A. Gordon, M. L. Gorodetsky, S. E. Gossan, M. Gosselin, R. Gouaty, C. Graef, P. B. Graff, M. Granata, A. Grant, S. Gras, C. Gray, G. Greco, A. C. Green, R. J. S. Greenhalgh, P. Groot, H. Grote, S. Grunewald, G. M. Guidi, X. Guo, A. Gupta, M. K. Gupta, K. E. Gushwa, E. K. Gustafson, R. Gustafson, J. J. Hacker, B. R. Hall, E. D. Hall, G. Ham-mond, M. Haney, M. M. Hanke, J. Hanks, C. Hanna, M. D. Hannam, J. Hanson, T. Hardwick, J. Harms, G. M. Harry, I. W. Harry, M. J. Hart, M. T. Hartman, C.-J. Haster, K. Haughian, J. Healy, J. Heefner, A. Heidmann, M. C. Heintze, G. Heinzl, H. Heitmann, P. Hello, G. Hem-ming, M. Hendry, I. S. Heng, J. Hennig, A. W. Heptonstall, M. Heurs, S. Hild, D. Hoak, K. A. Hodge, D. Hofman, S. E. Hollitt, K. Holt, D. E. Holz, P. Hopkins, D. J. Hosken, J. Hough, E. A. Houston, E. J. Howell, Y. M. Hu, S. Huang, E. A. Huerta, D. Huet, B. Hughey, S. Husa, S. H. Huttner, T. Huynh-Dinh, A. Idrisy, N. Indik, D. R. Ingram, R. Inta, H. N. Isa, J.-M. Isac, M. Isi, G. Islas, T. Isogai, B. R. Iyer, K. Izumi, M. B. Jacobson, T. Jacqmin, H. Jang, K. Jani, P. Jaranowski, S. Jawahar, F. Jiménez-Forteza, W. W. Johnson, N. K. Johnson-McDaniel, D. I. Jones, R. Jones, R. J. G. Jonker, L. Ju, K. Haris, C. V. Kalaghatgi, V. Kalogera, S. Kand-hasamy, G. Kang, J. B. Kanner, S. Karki, M. Kasprzack, E. Katsavounidis, W. Katzman, S. Kaufer, T. Kaur, K. Kawabe, F. Kawazoe, F. Kéfélian, M. S. Kehl, D. Keitel, D. B. Kel-ley, W. Kells, R. Kennedy, D. G. Keppel, J. S. Key, A. Khalaidovski, F. Y. Khalili, I. Khan, S. Khan, Z. Khan, E. A. Khazanov, N. Kijbunchoo, C. Kim, J. Kim, K. Kim, Nam-Gyu Kim,

Namjun Kim, Y.-M. Kim, E. J. King, P. J. King, D. L. Kinzel, J. S. Kissel, L. Kleybolte, S. Klimenko, S. M. Koehlenbeck, K. Kokeyama, S. Koley, V. Kondrashov, A. Kontos, S. Koranda, M. Korobko, W. Z. Korth, I. Kowalska, D. B. Kozak, V. Kringel, B. Krishnan, A. Królak, C. Krueger, G. Kuehn, P. Kumar, R. Kumar, L. Kuo, A. Kutynia, P. Kwee, B. D. Lackey, M. Landry, J. Lange, B. Lantz, P. D. Lasky, A. Lazzarini, C. Lazzaro, P. Leaci, S. Leavey, E. O. Lebigot, C. H. Lee, H. K. Lee, H. M. Lee, K. Lee, A. Lenon, M. Leonardi, J. R. Leong, N. Leroy, N. Letendre, Y. Levin, B. M. Levine, T. G. F. Li, A. Libson, T. B. Littenberg, N. A. Lockerbie, J. Logue, A. L. Lombardi, L. T. London, J. E. Lord, M. Lorenzini, V. Lorette, M. Lormand, G. Losurdo, J. D. Lough, C. O. Lousto, G. Lovelace, H. Lück, A. P. Lundgren, J. Luo, R. Lynch, Y. Ma, T. MacDonald, B. Machenschalk, M. MacInnis, D. M. Macleod, F. Magaña-Sandoval, R. M. Magee, M. Mageswaran, E. Majorana, I. Maksimovic, V. Malvezzi, N. Man, I. Mandel, V. Mandic, V. Mangano, G. L. Mansell, M. Manske, M. Mantovani, F. Marchesoni, F. Marion, S. Márka, Z. Márka, A. S. Markosyan, E. Maros, F. Martelli, L. Martellini, I. W. Martin, R. M. Martin, D. V. Martynov, J. N. Marx, K. Mason, A. Masserot, T. J. Massinger, M. Masso-Reid, F. Matichard, L. Matone, N. Mavalvala, N. Mazumder, G. Mazzolo, R. McCarthy, D. E. McClelland, S. McCormick, S. C. McGuire, G. McIntyre, J. McIver, D. J. McManus, S. T. McWilliams, D. Meacher, G. D. Meadors, J. Meidam, A. Melatos, G. Mendell, D. Mendoza-Gandara, R. A. Mercer, E. Merilh, M. Merzougui, S. Meshkov, C. Messenger, C. Messick, P. M. Meyers, F. Mezzani, H. Miao, C. Michel, H. Middleton, E. E. Mikhailov, L. Milano, J. Miller, M. Millhouse, Y. Minenkov, J. Ming, S. Mirshekari, C. Mishra, S. Mitra, V. P. Mitrofanov, G. Mitselmakher, R. Mittleman, A. Moggi, M. Mohan, S. R. P. Mohapatra, M. Montani, B. C. Moore, C. J. Moore, D. Moraru, G. Moreno, S. R. Morris, K. Mossavi, B. Mours, C. M. Mow-Lowry, C. L. Mueller, G. Mueller, A. W. Muir, Arunava Mukherjee, D. Mukherjee, S. Mukherjee, N. Mukund, A. Mullavey, J. Munch, D. J. Murphy, P. G. Murray, A. Mytidis, I. Nardecchia, L. Naticchioni, R. K. Nayak, V. Nacula, K. Nedkova, G. Nelemans, M. Neri, A. Neunzert, G. Newton, T. T. Nguyen, A. B. Nielsen, S. Nissanke, A. Nitz, F. Nocera, D. Nolting, M. E. N. Normandin, L. K. Nuttall, J. Oberling, E. Ochsner, J. O'Dell, E. Oelker, G. H. Ogin, J. J. Oh, S. H. Oh, F. Ohme, M. Oliver, P. Oppermann, Richard J. Oram, B. O'Reilly, R. O'Shaughnessy, C. D. Ott, D. J. Ottaway, R. S. Ottens, H. Overmire, B. J. Owen, A. Pai, S. A. Pai, J. R. Palamos, O. Palashov, C. Palomba, A. Pal-Singh, H. Pan, Y. Pan, C. Pankow, F. Pannarale, B. C. Pant, F. Paoletti, A. Paoli, M. A. Papa, H. R. Paris, W. Parker, D. Pascucci, A. Pasqualetti, R. Passaquieti, D. Passuello, B. Patricelli, Z. Patrick, B. L. Pearlstone, M. Pedraza, R. Pedurand, L. Pekowsky, A. Pele, S. Penn, A. Perreca, H. P. Pfeiffer, M. Phelps, O. Piccinni, M. Pichot, M. Pickenpack, F. Piergiovanni, V. Pierro, G. Pillant, L. Pinard, I. M. Pinto, M. Pitkin, J. H. Poeld, R. Poggiani, P. Popolizio, A. Post, J. Powell, J. Prasad, V. Predoi, S. S. Premachandra, T. Prestegard, L. R. Price, M. Prijatelj, M. Principe, S. Privitera, R. Prix, G. A. Prodi, L. Prokhorov, O. Puncken, M. Punturo, P. Puppato, M. Pürrer, H. Qi, J. Qin, V. Quetschke,

E. A. Quintero, R. Quitzow-James, F. J. Raab, D. S. Rabeling, H. Radkins, P. Raffai, S. Raja, M. Rakhmanov, C. R. Ramet, P. Rapagnani, V. Raymond, M. Razzano, V. Re, J. Read, C. M. Reed, T. Regimbau, L. Rei, S. Reid, D. H. Reitze, H. Rew, S. D. Reyes, F. Ricci, K. Riles, N. A. Robertson, R. Robie, F. Robinet, A. Rocchi, L. Rolland, J. G. Rollins, V. J. Roma, J. D. Romano, R. Romano, G. Romanov, J. H. Romie, D. Rosińska, S. Rowan, A. Rüdiger, P. Ruggi, K. Ryan, S. Sachdev, T. Sadecki, L. Sadeghian, L. Salconi, M. Saleem, F. Salemi, A. Samajdar, L. Sammut, L. M. Sampson, E. J. Sanchez, V. Sandberg, B. Sandeen, G. H. Sanders, J. R. Sanders, B. Sassolas, B. S. Sathyaprakash, P. R. Saulson, O. Sauter, R. L. Savage, A. Sawadsky, P. Schale, R. Schilling, J. Schmidt, P. Schmidt, R. Schnabel, R. M. S. Schofield, A. Schönbeck, E. Schreiber, D. Schuette, B. F. Schutz, J. Scott, S. M. Scott, D. Sellers, A. S. Sengupta, D. Sentenac, V. Sequino, A. Sergeev, G. Serna, Y. Setyawati, A. Seigny, D. A. Shaddock, T. Shaffer, S. Shah, M. S. Shahriar, M. Shaltev, Z. Shao, B. Shapiro, P. Shawhan, A. Sheperd, D. H. Shoemaker, D. M. Shoemaker, K. Siellez, X. Siemens, D. Sigg, A. D. Silva, D. Simakov, A. Singer, L. P. Singer, A. Singh, R. Singh, A. Singhal, A. M. Sintes, B. J. J. Slagmolen, J. R. Smith, M. R. Smith, N. D. Smith, R. J. E. Smith, E. J. Son, B. Sorazu, F. Sorrentino, T. Souradeep, A. K. Srivastava, A. Staley, M. Steinke, J. Steinlechner, S. Steinlechner, D. Steinmeyer, B. C. Stephens, S. P. Stevenson, R. Stone, K. A. Strain, N. Straniero, G. Stratta, N. A. Strauss, S. Strigin, R. Sturani, A. L. Stuver, T. Z. Summerscales, L. Sun, P. J. Sutton, B. L. Swinkels, M. J. Szczepańczyk, M. Tacca, D. Talukder, D. B. Tanner, M. Tápai, S. P. Tarabrin, A. Taracchini, R. Taylor, T. Theeg, M. P. Thirugnanasambandam, E. G. Thomas, M. Thomas, P. Thomas, K. A. Thorne, K. S. Thorne, E. Thrane, S. Tiwari, V. Tiwari, K. V. Tokmakov, C. Tomlinson, M. Tonelli, C. V. Torres, C. I. Torrie, D. Töyrä, F. Travasso, G. Traylor, D. Trifirò, M. C. Tringali, L. Trozzo, M. Tse, M. Turconi, D. Tuyenbayev, D. Ugolini, C. S. Unnikrishnan, A. L. Urban, S. A. Usman, H. Vahlbruch, G. Vajente, G. Valdes, M. Vallisneri, N. van Bakel, M. van Beuzekom, J. F. J. van den Brand, C. Van Den Broeck, D. C. Vander-Hyde, L. van der Schaaf, J. V. van Heijningen, A. A. van Veggel, M. Vardaro, S. Vass, M. Vasúth, R. Vaulin, A. Vecchio, G. Vedovato, J. Veitch, P. J. Veitch, K. Venkateswara, D. Verkindt, F. Vetrano, A. Viceré, S. Vinciguerra, D. J. Vine, J.-Y. Vinet, S. Vitale, T. Vo, H. Vocca, C. Vorvick, D. Voss, W. D. Voursden, S. P. Vyatchanin, A. R. Wade, L. E. Wade, M. Wade, S. J. Waldman, M. Walker, L. Wallace, S. Walsh, G. Wang, H. Wang, M. Wang, X. Wang, Y. Wang, H. Ward, R. L. Ward, J. Warner, M. Was, B. Weaver, L.-W. Wei, M. Weinert, A. J. Weinstein, R. Weiss, T. Welborn, L. Wen, P. Weßels, T. Westphal, K. Wette, J. T. Whelan, S. E. Whitcomb, D. J. White, B. F. Whiting, K. Wiesner, C. Wilkinson, P. A. Willems, L. Williams, R. D. Williams, A. R. Williamson, J. L. Willis, B. Willke, M. H. Wimmer, L. Winkelmann, W. Winkler, C. C. Wipf, A. G. Wiseman, H. Wittel, G. Woan, J. Worden, J. L. Wright, G. Wu, J. Yablon, I. Yakushin, W. Yam, H. Yamamoto, C. C. Yancey, M. J. Yap, H. Yu, M. Yvert, A. Zadrożny, L. Zangrando, M. Zanolin, J.-P. Zendri, M. Zevin, F. Zhang, L. Zhang, M. Zhang, Y. Zhang, C. Zhao, M. Zhou,

- Z. Zhou, X. J. Zhu, M. E. Zucker, S. E. Zuraw, and J. Zweizig. Observation of Gravitational Waves from a Binary Black Hole Merger. *Physical Review Letters*, 116(6):061102, February 2016.
- [28] Zin Lin, Xiangdong Liang, Marko Lončar, Steven G. Johnson, and Alejandro W. Rodriguez. Cavity-enhanced second-harmonic generation via nonlinear-overlap optimization. *Optica*, 3(3):233–238, March 2016.
- [29] Joshua McNeur et al. Elements of a dielectric laser accelerator. *arXiv preprint arXiv:1604.07684*, 2016.
- [30] K Mizuno et al. Experimental evidence of the inverse Smith–Purcell effect. *Nature*, 328(6125):45–47, 1987.
- [31] Sean Molesky, Zin Lin, Alexander Y. Piggott, Weiliang Jin, Jelena Vucković, and Alejandro W. Rodriguez. Inverse design in nanophotonics. *Nature Photonics*, 12(11):659, November 2018.
- [32] P Musumeci et al. High energy gain of trapped electrons in a tapered, diffraction-dominated inverse-free-electron laser. *Phys. Rev. Lett.*, 94(15):154801, 2005.
- [33] Jorge Nocedal. Updating quasi-Newton matrices with limited storage. *Math. Comput.*, 35(151):773–782, 1980.
- [34] M. Necat Ozisik. *Inverse Heat Transfer : Fundamentals and Applications*. Routledge, May 2018.
- [35] E. A. Peralta et al. Demonstration of electron acceleration in a laser-driven dielectric microstructure. *Nature*, 503(7474):91–94, 2013.
- [36] Alexander Y. Piggott, Jesse Lu, Konstantinos G. Lagoudakis, Jan Petykiewicz, Thomas M. Babinec, and Jelena Vučković. Inverse design and demonstration of a compact and broadband on-chip wavelength demultiplexer. *Nature Photonics*, 9(6):374–377, June 2015.
- [37] T Plettner and RL Byer. Microstructure-based laser-driven free-electron laser. *Nucl. Instrum. Methods Phys. Res., Sect. A*, 593(1):63–66, 2008.
- [38] T Plettner et al. Proposed few-optical cycle laser-driven particle accelerator structure. *Phys. Rev. ST Accel. Beams*, 9(11):111301, 2006.
- [39] C. R Pollock and Michal Lipson. *Integrated photonics*. Kluwer Academic, Norwell, Mass., 2010. OCLC: 854553854.
- [40] Aaswath P. Raman, Marc Abou Anoma, Linxiao Zhu, Eden Rephaeli, and Shanhui Fan. Passive radiative cooling below ambient air temperature under direct sunlight. *Nature*, 515(7528):540–544, November 2014.

- [41] Wonseok Shin and Shanhui Fan. Choice of the perfectly matched layer boundary condition for frequency-domain Maxwell's equations solvers. *J. Comput. Phys.*, 231(8):3406–3431, 2012.
- [42] Ole Sigmund. Systematic Design of Metamaterials by Topology Optimization. In R. Pyrz and J. C. Rauhe, editors, *IUTAM Symposium on Modelling Nanomaterials and Nanosystems*, IUTAM Bookseries, pages 151–159. Springer Netherlands, 2009.
- [43] Ken Soong et al. Laser damage threshold measurements of optical materials for direct laser accelerators. *AIP Conf. Proc.*, 1507(1):511–515, 2012.
- [44] Allen Taflove and Susan C Hagness. *Computational Electrodynamics: The Finite-Difference Time-Domain Method*. Artech House Publishers, Norwood, MA, 2nd edition, 2000.
- [45] Masataka Tanaka and G. S. Dulikravich. *Inverse Problems in Engineering Mechanics*. Elsevier, November 1998. Google-Books-ID: tyOpk49g0vsC.
- [46] N. H. E. Weste and K. Eshraghian. Principles of CMOS VLSI design: A systems perspective. *NASA STI/Recon Technical Report A*, 85, 1985.
- [47] Darrell Whitley. A genetic algorithm tutorial. *Statistics and Computing*, 4(2):65–85, June 1994.
- [48] Zongfu Yu, Aaswath Raman, and Shanhui Fan. Fundamental limit of nanophotonic light trapping in solar cells. *Proceedings of the National Academy of Sciences*, 107(41):17491–17496, October 2010.
- [49] T B Zhang et al. Stimulated dielectric wake-field accelerator. *Phys. Rev. E*, 56(4):4647, 1997.